Applied Chemical Engineering (2024) Volume 7 Issue 1
doi: 10.24294/ace.v7i1.2284

ORIGINAL RESEARCH ARTICLE

Carbenes trapping on Aluminum-Magnesium surface implanted with Silicon, Germanium, Tin: Promising of semiconductors by molecular modeling approach

Fatemeh Mollaamin[1,*], Majid Monajjemi[2]

[1] *Department of Biomedical Engineering, Faculty of Engineering and Architecture, Kastamonu University, Kastamonu 37150, Turkey*

[2] *Department of Chemical Engineering, Central Tehran Branch, Islamic Azad University, Tehran 1496969191, Iran*

*** Corresponding author:** Fatemeh Mollaamin, smollaamin@gmail.com

ABSTRACT

Al-Mg surface doped silicon, germanium and tin is theoretically studied using first-principles density functional theory (DFT) at the CAM-B3LYP/EPR-III, LANL2DZ,6-31+G(d,p) level of theory to explore the chemical adsorption and corrosion inhibition of organic carbenes through coating process. The fluctuation of NQR is estimated the inhibiting role of pyridine and its derivatives (picoline, 3-picoline,4-picoline,2,4-lutidine) for (Si, Ge, Sn)-doped Al-Mg alloy nanosheet due to concerning nitrogen in the benzene ring of related heterocyclic compounds becoming close to the monolayer nanosurface of Al-Mg-X (X = Si, Ge, Sn) nanoalloys. The NMR spectroscopy remarks that (Si, Ge, Sn)-doped Al-Mg alloy nanosheet has maximum band wavelengths approximately between 10 ppm–2000 ppm accompanying the sharpest peaks for inhibitors → Al-Mg-X which are between 10 ppm–100 ppm. IR spectroscopy has exhibited that (Si, Ge, Sn)-doped Al-Mg alloy nanosheet with the fluctuation in the frequency of intra-atomic interaction leads us to the most influence in the vicinage atoms generated due to inter-atomic interaction. The maximum IR spectrum for complexes of [inhibitor → Al-Mg-X (X = Si, Ge, Sn)] is observed in the frequency range between 500 cm^{-1}–3500 cm^{-1}. This work exhibits that proper monitoring of the coating mechanism by Langmuir adsorption can illustrate inhibiting the aluminum nanoalloys corrosion through an investigation of their structural and thermodynamic properties. This work investigates the characteristics, band structure, and projected density of state (PDOS) of Al-Mg nanoalloy doped with Si, Ge, Sn elements for increasing the corrosion inhibition of the surface through adsorption of organic molecules of carbenes in the surface coatings process. This article can be helpful in a range of applications which uses Al-Mg alloy for the study of energy storage and adsorption of air pollution or water contamination. Many different approaches such as surface coatings, alloying and doping can be adopted to protect the surface.

Keywords: Al-Mg-Si; Al-Mg-Ge; Al-Mg-Sn; DFT; CAM-B3LYP

ARTICLE INFO

Received: 22 June 2023
Accepted: 25 September 2023
Available online: 14 December 2023

1. Introduction

Aluminum nanoalloys (Al-Mg) have been the principle compounds applied for airframe structures until the enhancing tendency in the application of composites of the polymer matrix. Aluminum-Mg nanoalloys are thinner than further aluminum nanoalloys and much less fulminant than other nanoalloys consisting of large values of Mg. Aluminum-Si is one of the most significant aluminum nanoalloys with vast contents of Si in foundry and has a great finiteness of usages in the air activities through a best mixture of micromechanical economy[1–5].

Si element in aluminum-silicon based foundry nanoalloys impacts expandable characteristics at different temperatures, but its

function appears more important in lack of nanoalloy metals such as Mg, Fe and Cu[5]. However, the interactions between solute atoms and vacancies in Al-Mg-Ge nanoalloys are not vivid. Among the various methods that minimize corrosion of metal surface, its inhibition by organic molecules is one of the most applicable methods because of its stability and low cost[6–16].

The aim of this paper is the application of heterocyclic materials as corrosive inhibitors for Al and its nanoalloys. Because diverse characteristics of organic structures are to be represented, it is essential that the electrons of a set of organic structures be discussed[17–19]. Therefore, operated organic compounds as corrosion stoppers were chosen and determined on the basis of their physicochemical characteristics[20,21] and relatively little consideration has been dedicated to the quantitative estimation of the internal and steric influence of these compounds upon their inhibition yield. In other works, it has been studied the interaction between imidazole and the aluminum surface which is often employed in experimental researches[22–39].

The microscopic interaction and reaction mechanism between molecules could be profoundly disclosed from the quantum chemical characteristics, which prepare a beneficial path to find adsorption attitude between molecules and interfaces at the atomic and molecular stages[40–45]. It has been studied that pyridine family compounds have been broadly applied through their intense polarity and increasing potency in ionic liquids and solution. It is seen that some compounds including nicotine-amide, pyridine-2-formamide and pyridine-4-formamide can be employed as efficient increasing agents for electro-deposition of aluminum in [Bmim] Cl/AlCl3 with the unclear mechanism in finding the intermolecular interaction between additives and electrode, charge distribution, and adsorption comportment[42].

The interaction of magnesium microstructure, and embedding with other atoms applying the density functional theory (DFT) approach, was studied among scientist. The first-principle analysis of the charge transfer in magnesium corrosion by mixing water molecules in their structure was investigated[46]. Furthermore, the researchers used the DFT approach for calculation of Al-Cu-Mg nanoalloys, which led to stability effects during the addition of specific atom amounts in those alloys[47]. Then, the properties of Li, Al, and Cd-doped Mg alloys using a first-principle calculation to calculate the cohesive energy and its electronic structure were evaluated[22]. The results exhibited that Mg-Al alloy has the lowest cohesive energy and is the most stable alloy[48]. The DFT calculation was also used in other researches to illustrate the structure of water over metal surfaces; results showed that strong adsorption of the water molecule on the metal surface leads to weaker hydrogen bonding among the molecules[49,50]. It was also DFT was used on stepped Pt surfaces which indicated that surfaces with a lower coordination number have a higher intention to adsorb water molecules[51–53]. It was presented an analogous adsorption manner for water clusters on both flat and stepped transition metal surfaces[54,55]. The thermodynamic behavior of dissolution in the alloy sheets of transition metals on the basis of DFT calculations was investigated[56].

Among various approaches to improve the sensing performance of alloy surfaces, the metal-doped method is perceived as effective, and has received great attention and is widely investigated. However, it is still a challenge to construct heterogeneous non-metal/metalloid/metal-doped surface with an excellent sensing performance.

The present work intends to accomplish an extension of the previous works[45] of the role of pyridine and its family compounds as corrosion inhibitor for aluminum nanoalloys which have been generated by adding some elements including Si, Ge, and Sn to Al-Mg nanoalloy and forming the Al-Mg-X (X = Si, Ge, Sn) nanoalloys surface. These complexes have been investigated using NMR, IR, and NQR spectroscopy.

2. Theoretical insights, applied material and method

2.1. Aluminum nanoalloys

Light weight or corrosion resistance of aluminum nanoalloys make them suitable in engineering structures and components. The particular components for nanoalloying of Al element are copper, magnesium, manganese, silicon, tin, nickel and zinc[57,58].

The lattice of Nanoalloys of Al-Mg-Si gets supersaturated with solute in the room temperature. These atoms will enter into small the clusters on the aluminum lattice. After a short time at the high temperature, appropriate clusters start reorganizing into periodic constructions (**Scheme 1a**)[59–61]. Triple Al nanoalloys of Al-Mg-Si are extendedly applied as car bodies replacing heavier metals related to the economic pressure which needs the decrease of CO_2 emission and fuel consumption. Al-Si nanoalloys without Cu additions are employed when appropriate corrosion resistance is needed. So, Mg is able to replace with Cu. In fact, Mg and Si can produce the intermetallic hardening phase Mg_2Si which precipitates in the α-aluminum matrix and enhances the efficiency of resistance. The principal restrictions of the triple nanoalloy of aluminum-magnesium-silicon cast ingredients are because of the remarkable impact of the solidity situations on the final microstructure. The final cast ingredients unavoidably consists of a determined number of defects like oxide films, shrinkage and gas porosity, which impress the exhaustion behavior and the mechanical parameters[62–67].

In some researches, the precipitation in an Al-Mg-Ge nanoalloy (**Scheme 1b**) has been studied applying annular dark field scanning TEM (ADF-STEM) and high-resolution transmission electron microscopy (HRTEM). The fine precipitates had forms including a near-hexagonal network of Ge atoms with sub-cell dimensions a = b ≈ 0.405 nm, c = 0.405 nm which is very identical to the Si network that relates all precipitate constructions in the Al-Mg-Si nanoalloys and its equilibrium phase is β-Mg_2Ge corresponds to its phase diagram. In some investigations, the precipitation sequence of Al-Mg-Ge nanoalloys consisting of various components of Mg_2Ge has been studied by TEM and HRTEM observation and hardness test for finding the impact of Mg_2Ge components on age-hardening treatment of the nanoalloys[68–72].

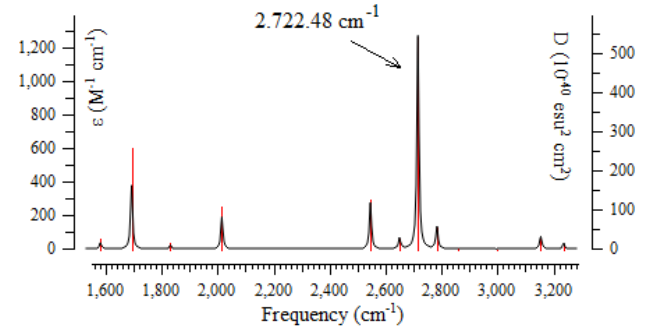

(a)

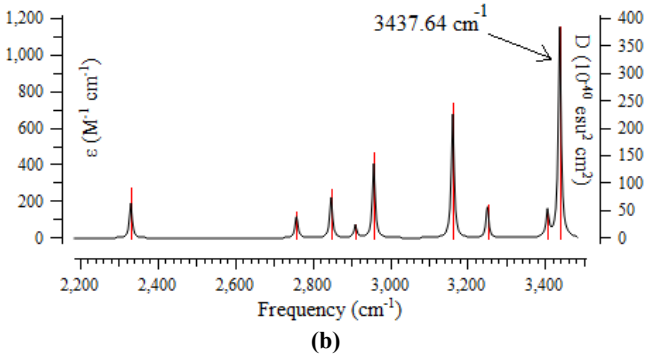

(b)

Scheme 1. (*Continued*).

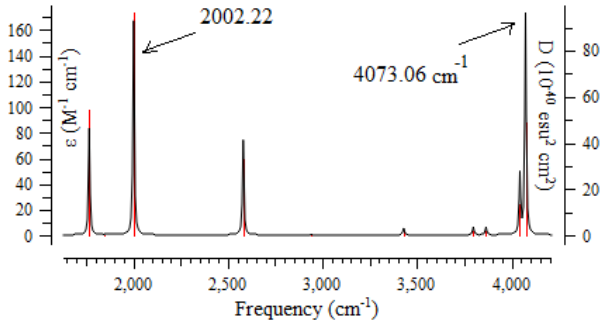

Scheme 1. IR spectra for aluminum nanoalloys (Al-Mg-X) consisting of **(a)** Al-Mg-Si; **(b)** Al-Mg-Ge; and **(c)** Al-Mg-Sn.

Moreover, the frequency range of IR spectrum for each compounds in **Scheme 1** has been shown in the maximum frequency approximately between 1500 cm^{-1}–4500 cm^{-1}, for Al-Mg-X (X = Si, Ge, Sn), concerning the strongest peaks about 2722 cm^{-1} (**Scheme 1a**), for Al-Mg-Si, 3437.64 cm^{-1} for Al-Mg-Ge (**Scheme 1b**), and 2002.22 cm^{-1}, 4073.06 cm^{-1} for Al-Mg-Sn (**Scheme 1c**).

2.2. Corrosion resistance increment by nanoalloy ingredients

Al-nanoalloy with high corrosion resistance of that is related to a thin but very tight and tightly holding layer of Al oxide produced on the surface of the compound which defends the material against further oxidation. But, despite these attractive properties, in the existence of offensive ions such as chloride and halide, the protective layer might be locally ruined, and a corrosive attack happens[73]. The principal corrosion trouble accompanied with Al and its nanoalloys relates to the localized breakdown of the inactive film which conducts to the start and increase of corrosion cavities in a chloride medium[74].

Aluminum nanoalloys can be susceptible to intergranular corrosion if second-phase micro constituents are formed at grain boundaries. A corrosion potential of the nanoalloy different from that of the matrix will also cause intergranular corrosion. The presence of appreciable amounts of soluble alloying elements, such as Cu, Mg, Si, and Zn, will make these nanoalloys susceptible to stress-corrosion cracking[75].

Some of the common types of corrosion for Al which are independent of the corrosive environment consist of pitting, stress-corrosion cracking, exfoliation, intergranular, and galvanic[75]. The non-heat treatable nanoalloys have a higher corrosion resistance toward general corrosion compared to the heat treatable nanoalloys. However, the nanoalloys containing the Al-Mg_2Si system also show considerable resistance to general corrosion. The same behavior is observed for the nanoalloys that do not contain copper (Al-Zn-Mg). The nanoalloys' resistance to pitting corrosion increases significantly with increasing purity[76].

2.3. Three-layer ONIOM method

In theoretical ONIOM method, any combination of three levels in the reducing order of accuracy can be accepted in ONIOM3 with three level of high [QM1/ab-intio, DFT], medium [QM2/semi-empirical], and low [QM3/MM] (**Scheme 2**)[77–82].

In this research, the mixing of three levels of QM1, QM2 and QM3 in reducing order of accuracy has been assigned containing high, medium, and low levels of theory[83]:

$$E_{\mathrm{ONIOM}} = E_{\mathrm{high(QM1)}} + E_{\mathrm{medium(QM2)}} + E_{\mathrm{low(QM3)}} \quad (1)$$

The ONIOM method could be lightly extended and popularized to an *n*-layer method[84]:

$$E_{\mathrm{ONIOM}n} = \sum_{i=1}^{n} E[\mathrm{level}\ (i), \mathrm{model}\ (n+1-i)] - \sum_{i=2}^{n} E[\mathrm{level}\ (i), \mathrm{model}\ (n+2-i)] \quad (2)$$

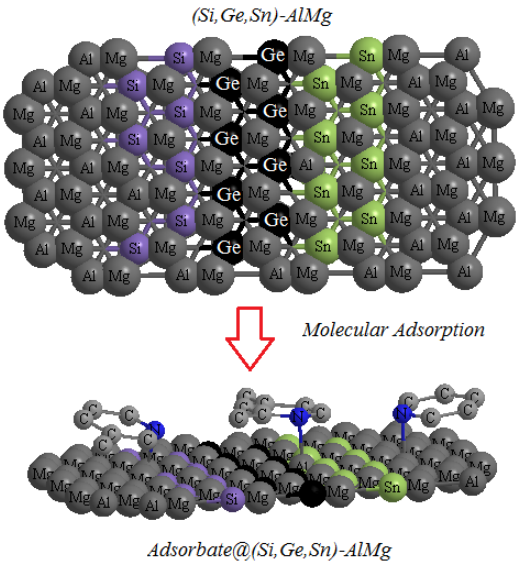

Scheme 2. Process of physical and chemical adsorption of pyridine, 2-picolone, 3-picoline, 4-picoline and 2,4-lutidine onto Aluminum nanoalloy in different levels containing high, medium and low levels by theoretical ONIOM method of calculation.

The three-layer method of ONIOM permits us to investigate a larger system more precisely than the one-layered model which can treat a medium size system very accurately like a very large system with modest accuracy[85]. This three-layer model has been employed to activate barriers for the pyridine, 2-picoline, 3-picoline, 4-picoline and 2,4-lutidine onto mono-layer Al-X (X = Al, Mg, Ga, Si) surface toward forming the Langmuir adsorption complexes including pyridine → Al-Mg-Si, pyridine → Al-Mg-Ge, pyridine → Al-Mg-Sn; 2-picoline → Al-Mg-Si, 2-picoline → Al-Mg-Ge, 2-picoline → Al-Mg-Sn; 3-picoline → Al-Mg-Si, 3-picoline → Al-Mg-Ge, 3-picoline → Al-Mg-Sn; 4-picoline → Al-Mg-Si, 4-picoline → Al-Mg-Ge, 4-picoline → Al-Mg-Sn; and 2,4-lutidine → Al-Mg-Si, 2,4-lutidine → Al-Mg-Ge, 2,4-lutidine → Al-Mg-Sn (**Scheme 2**).

2.4. Theory of Langmuir adsorption

The Langmuir isotherm is extremely applied in the identification of inhibitor adsorption status specification and it is represented as follows[86]:

$$\frac{C_{inh}}{\theta} = \frac{1}{K_{ads}} + C_{inh} \tag{3}$$

where C_{inh} is the inhibitor concentration; θ is the fractional coverage of the steel surface and K_{ads} is the equilibrium constant of the adsorption and desorption procedures[87].

$$\Delta G^{o}_{ads} = -RT\ln(55.5K_{ads}) \tag{4}$$

where R is the gas constant (8314 $JK^{-1}mol^{-1}$), T is the absolute temperature (T) and the value 55.55 (mol^{-1}) is the concentration of water in solution.

The pyridine, 2-picoloine,3-picoline, 4-picoline and 2,4-lutidine as corrosion inhibitors on the triple aluminum nanoalloys surface containing Al-Mg-Si, Al-Mg-Ge, and Al-Mg-Sn have been observed (**Scheme 2**).

2.5. Theoretical method of density functional theory (DFT)

The Hohenberg-Kohn (HK) functions have severely made the electronic density admissible as basic variable to electronic and structure calculations. On the other hand, progress the practical DFT approaches only became remarkable after Kohn and Sham published their famous set of equations which are represented as Kohn-Sham (KS) equations[88–102].

Density functional theory (DFT) calculations have been performed using Gaussian 16 revision C.01[103]

software. The input files for the corrosion inhibitors adsorbed onto the Al-Mg-Si, Al-Mg-Ge, and Al-Mg-Sn surfaces (**Scheme 1**) have been prepared with GaussView 6.1[104] due to the rigid system and Z-Matrix format of which a blank line has been placed and using LANL2DZ,EPR-III, 6-31+G(d,p) basis sets to determine chemical shielding, frequencies, occupancy and hybrid of natural atomic orbitals, electrostatic potential, electronic potential, energy gap of frontier orbitals, natural atomic charges, electron density mapping, and other quantum properties for this investigation. The rigid PES has been run at CAM-B3LYP/EPR-III, LANL2DZ, 6-31+G(d,p) for pyridine and its family (2-picoline, 3-picoline, 4-picoline and 2,4-lutidine) adsorbed onto aluminum and its nanoalloys.

3. Results and discussion

Adsorbing pyridine and its family as heterocyclic corrosion inhibitors on the Al-Mg-X (X = Si, Ge, Sn) nanoalloys surface in NaCl solution approve by the most suitable Langmuir isotherm (**Scheme 2**).

3.1. Nuclear magnetic resonance

The NMR data of isotropic (σ_{iso}) and anisotropic shielding tensor (σ_{aniso}) for some metal atoms (Al, Mg, Si, Ge, Sn) participating in interatomic interaction with inhibitors and intra-atomic with themselves estimate by Gaussian 16 revision C.01 program software[103] and represent in **Table 1**.

Table 1. NMR properties of σ_{iso} and σ_{aniso} of metal atoms for Al-Mg-X (X = Si, Ge, Sn) nanoalloys surface in ppm which have been coated by pyridine, 2-picoline, 3-picoline, 4-picoline , and 2,4-lutidine.

Pyridine → Al-Mg-Si												
ppm	Al7	Mg8	Si9	Mg10	Al11	Mg12	Al13	Si14	Al15	Si16	Mg17	Al18
σ_{iso}	619.45	827.59	201.63	436.94	658.21	786.47	758.82	373.33	463.06	308.64	291.11	123.53
σ_{aniso}	800.53	337.29	1044.88	451.02	691.46	538.17	845.76	561.66	1205.85	1682.51	857.32	1829.51
Pyridine → Al-Mg-Ge												
ppm	Al7	Mg8	Ge9	Mg10	Al11	Mg12	Al13	Ge14	Al15	Ge16	Mg17	Al18
σ_{iso}	639.03	768.50	1714.47	281.83	549.07	703.86	752.08	1489.20	616.03	1023.15	202.15	93.80
σ_{aniso}	695.25	326.45	978.15	597.09	679.09	338.51	459.01	1362.93	845.31	1733.32	765.66	1652.22
Pyridine → Al-Mg-Sn												
ppm	Al7	Mg8	Sn9	Mg10	Al11	Mg12	Al13	Sn14	Al15	Sn16	Mg17	Al18
σ_{iso}	795.26	785.86	4212.92	405.20	547.50	722.13	790.10	4403.13	716.31	4151.35	468.21	578.28
σ_{aniso}	467.52	335.81	1497.96	755.24	435.82	436.32	329.44	564.75	460.63	1399.02	491.62	499.38
2-picoline → Al-Mg-Si												
ppm	Al8	Mg9	Si10	Mg11	Al12	Mg13	Al14	Si15	Al16	Si17	Mg18	Al19
σ_{iso}	547.50	811.34	325.38	429.64	583.66	786.51	745.19	324.86	631.27	-336.12	302.92	197.84
σ_{aniso}	749.14	349.00	918.18	427.22	768.70	547.46	806.08	863.07	1085.79	1746.70	749.35	1770.22
2-picoline → Al-Mg-Ge												
ppm	Al8	Mg9	Ge10	Mg11	Al12	Mg13	Al14	Ge15	Al16	Ge17	Mg18	Al19
σ_{iso}	595.84	763.75	1868.86	309.32	570.59	710.52	733.08	1578.57	699.88	1031.16	238.00	210.18
σ_{aniso}	627.46	347.78	864.77	570.58	625.56	335.33	449.33	1465.55	626.70	1988.63	745.57	1379.96
2-picoline → Al-Mg-Sn												
ppm	Al8	Mg9	Sn10	Mg11	Al12	Mg13	Al14	Sn15	Al16	Sn17	Mg18	Al19
σ_{iso}	711.59	808.21	4060.17	355.29	569.23	721.75	699.53	4262.19	800.53	3821.24	402.70	340.94
σ_{aniso}	445.41	369.75	1423.99	694.78	546.22	375.06	377.64	918.10	391.11	1927.02	590.98	921.89

Table 1. (*Continued*).

3-picoline → Al-Mg-Si												
ppm	Al8	Mg9	Si10	Mg11	Al12	Mg13	Al14	Si15	Al16	Si17	Mg18	Al19
σ_{iso}	733.03	798.77	199.78	455.99	312.04	702.91	656.81	508.72	923.58	102.46	410.38	743.75
σ_{aniso}	745.05	378.25	971.75	593.99	358.88	435.08	836.79	1485.19	1284.65	1252.98	605.29	1902.23
3-picoline → Al-Mg-Ge												
ppm	Al8	Mg9	Ge10	Mg11	Al12	Mg13	Al14	Ge15	Al16	Ge17	Mg18	Al19
σ_{iso}	708.06	774.67	1648.50	429.07	379.48	664.96	624.80	1941.46	846.16	1327.04	376.30	684.07
σ_{aniso}	617.89	320.78	1503.76	524.68	346.88	235.91	510.45	1540.89	1298.03	1166.44	487.82	1054.43
3-picoline → Al-Mg-Sn												
ppm	Al8	Mg9	Sn10	Mg11	Al12	Mg13	Al14	Sn15	Al16	Sn17	Mg18	Al19
σ_{iso}	182.99	651.81	3900.49	203.22	445.28	655.20	172.06	3900.75	573.85	3178.76	449.78	314.73
σ_{aniso}	1163.02	316.16	3913.05	966.55	2235.32	428.80	1137.11	1567.85	794.32	5118.22	594.58	1040.78
4-picoline → Al-Mg-Si												
ppm	Al8	Mg9	Si10	Mg11	Al12	Mg13	Al14	Si15	Al16	Si17	Mg18	Al19
σ_{iso}	660.33	650.19	1773.56	593.12	600.43	650.63	889.35	631.37	659.12	847.34	7.00	1121.07
σ_{aniso}	1743.10	120.77	3537.62	1068.64	537.64	416.84	361.20	2067.32	2164.84	2986.28	1691.41	2968.60
4-picoline → Al-Mg-Ge												
ppm	Al8	Mg9	Ge10	Mg11	Al12	Mg13	Al14	Ge15	Al16	Ge17	Mg18	Al19
σ_{iso}	619.85	702.07	1241.25	391.16	660.95	594.26	868.76	1219.63	367.35	1306.15	39.88	378.92
σ_{aniso}	739.71	332.37	1493.86	444.18	609.94	457.60	191.57	2026.75	1189.31	2192.83	883.71	1044.62
4-picoline → Al-Mg-Sn												
ppm	Al8	Mg9	Sn10	Mg11	Al12	Mg13	Al14	Sn15	Al16	Sn17	Mg18	Al19
σ_{iso}	532.41	665.58	2808.10	231.23	737.28	707.70	733.92	4636.84	494.17	3482.18	299.83	270.21
σ_{aniso}	722.56	244.02	2123.19	1102.60	895.87	318.25	358.67	1063.81	2352.60	3346.55	819.46	676.12

Table 1. (*Continued*).

2,4-lutidine → Al-Mg-Si												
ppm	Al9	Mg10	Si11	Mg12	Al13	Mg14	Al15	Si16	Al17	Si18	Mg19	Al20
σ_{iso}	534.00	570.29	267.97	113.53	544.22	544.18	810.57	239.56	747.80	716.73	474.26	770.17
σ_{aniso}	794.01	370.10	1724.90	1165.43	554.93	196.40	449.00	1879.34	1819.60	2501.82	859.81	1249.52
2,4-lutidine → Al-Mg-Ge												
ppm	Al9	Mg10	Ge11	Mg12	Al13	Mg14	Al15	Ge16	Al17	Ge18	Mg19	Al20
σ_{iso}	894.19	753.17	1549.59	400.06	708.57	728.14	900.32	2619.47	817.67	1572.28	417.67	730.11
σ_{aniso}	648.07	330.70	1459.82	266.00	585.62	309.12	422.45	755.89	800.26	1438.71	383.47	1480.02
2,4-lutidine → Al-Mg-Sn												
ppm	Al9	Mg10	Sn11	Mg12	Al13	Mg14	Al15	Sn16	Al17	Sn18	Mg19	Al20
σ_{iso}	522.34	649.65	4337.03	416.52	6.66	754.56	609.79	4629.61	749.72	3647.98	290.98	395.20
σ_{aniso}	1849.17	282.48	1527.75	552.92	1405.52	330.11	837.73	1164.24	406.80	2470.95	750.37	1851.19

$$\sigma iso\ (\text{ppm}) = (\sigma 33 + \sigma 22 + \sigma 11)/3 \quad (5)$$

$$\sigma aniso\ (\text{ppm}) = \sigma 33 - (\sigma 22 + \sigma 11)/2 \quad (6)$$

The Gauge Invariant Atomic Orbital (GIAO) approach proposes as an accurate model for NMR computations, and ONIOM has achieved much attention for achieving NMR chemical shifts in inhibitor-surface complexes:

$$\sigma_{iso,ONIOM} = \sigma_{iso,high(QM1)} + \sigma_{iso,medium(QM2)} + \sigma_{iso,low(QM3)} \quad (7)$$

It presents that σ_{iso} and σ_{aniso} enhance with the occupancy and then the negative charge of nitrogen atom in pyridine and its derivatives diffusing onto Al-Mg-X (X = Si, Ge, Sn) nanoalloy surface (**Figure 1a–e**).

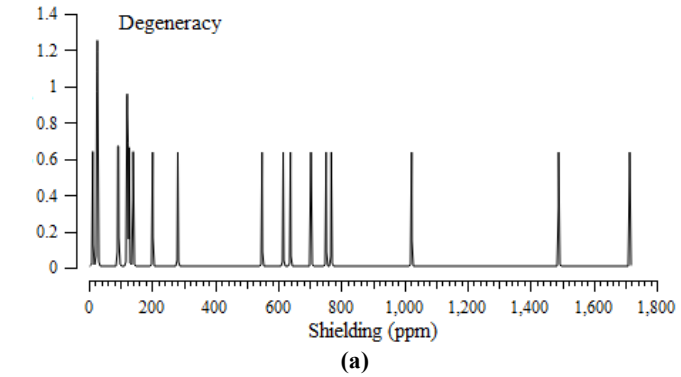

(a)

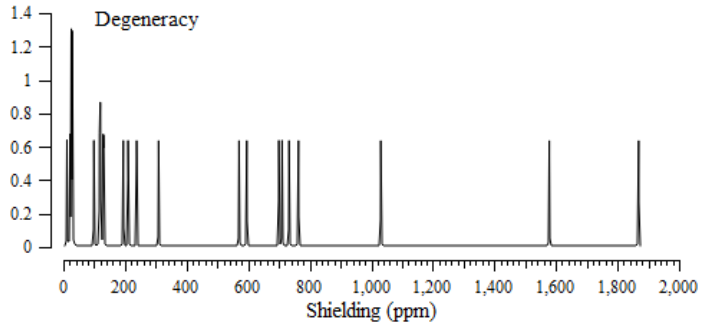

(b)

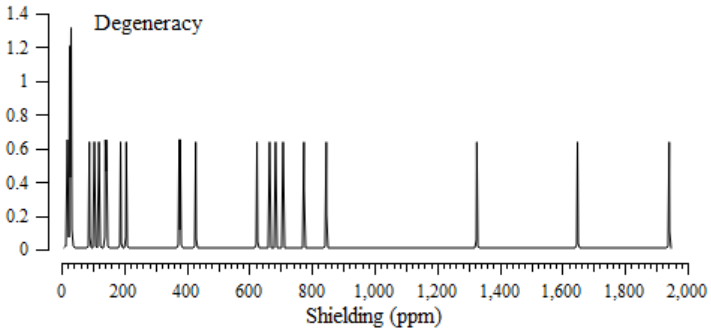

(c)

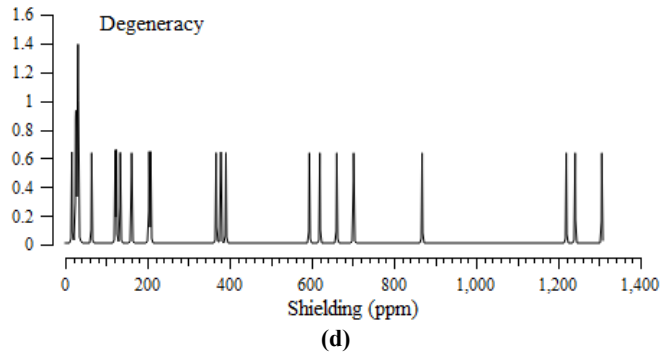

(d)

Figure 1. (*Continued*).

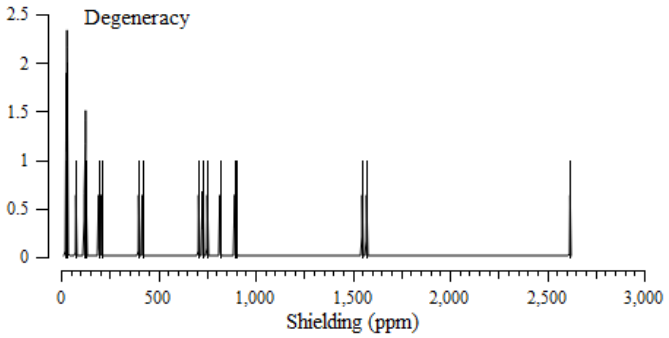

(e)

Figure 1. NMR spectroscopy for **(a)** pyridine → Al-Mg-X; **(b)** 2-picoline → Al-Mg-X; **(c)** 3-picoline → Al-Mg-X; **(d)** 4-picoline → Al-Mg-X; and **(e)** 2,4-lutidine → Al-Mg-X, by showing the active nitrogen atom in heterocyclic compounds becoming close to the nanosurface (X = Si, Ge, Sn).

Pyridine → Al-Mg-Si, pyridine → Al-Mg-Ge, pyridine → Al-Mg-Sn; 2-picoline → Al-Mg-Si, 2-picoline → Al-Mg-Ge, 2-picoline → Al-Mg-Sn; 3-picoline → Al-Mg-Si, 3-picoline → Al-Mg-Ge, 3-picoline → Al-Mg-Sn; 4-picoline → Al-Mg-Si, 4-picoline → Al-Mg-Ge, 4-picoline → Al-Mg-Sn; and 2,4-lutidine → Al-Mg-Si, 2,4-lutidine → Al-Mg-Ge, 2,4-lutidine → Al-Mg-Sn exhibit maximum band wavelengths approximately between 10 ppm–2000 ppm for these compounds (**Figure 1a–e**). In fact, the sharpest peaks for inhibitors → Al-Mg-X are approximately between 10 ppm–100 ppm (**Figure 1a–e**).

In fact, the adsorption of pyridine, 2-picoline, 3-picoline, 4-picoline and 2,4-lutidine molecules introduce spin polarization on the Al-Mg-X (X = Si, Ge, Sn) nanoalloy surfaces, indicating that it can be employed as a magnetic nitrogen heterocyclic sensor for these inhibitors detecting.

3.2. Nuclear quadrupole resonance (NQR)

In NMR, nuclei with spin ≥ 1/2 have a magnetic dipole moment so that their energies are split by a magnetic field, permitting resonance sorption of energy dependent on the Larmor frequency; $\omega_L = \gamma B$, where γ the gyromagnetic ratio is and B is the magnetic field external to the nucleus. As the EFG at the position of the nucleus in organic inhibitors is assigned by the valence electrons twisted in the special linkage with close nuclei of aluminum surface, the NQR frequency at which transitions happen is particular for an inhibitor → Al-Mg-X (X = Si, Ge, Sn) complex (**Table 2**).

Table 2. The electric potential for elements of pyridine and its privatives that have been adsorbed on the Al-Mg-Si/Ge/Sn surface by CAM-B3LYP/EPR-III,6-31+G(d,p) calculation extracted of NQR method. *Y = Al-Mg.

Atom type	Pyridine → *Y-Si	Atom type	Pyridine → *Y-Ge	Atom type	Pyridine →*Y-Sn
Al7	−43.7553	Al7	−43.7127	Al7	−43.7008
Mg8	−38.7059	Mg8	−38.6713	Mg8	−38.6524
Si9	−48.2934	Ge9	−153.2693	Sn9	−283.4296
Mg10	−38.9599	Mg10	−38.9070	Mg10	−38.8547
Al11	−43.7540	Al11	−43.7154	Al11	−43.6980
Mg12	−38.7213	Mg12	−38.6723	Mg12	−38.6283
Al13	−43.3077	Al13	−43.2488	Al13	−43.1719
Si14	−48.0553	Ge14	−153.0196	Sn14	−283.1590
Al15	−43.6037	Al15	−43.5209	Al15	−43.4337
Si16	−48.3099	Ge16	−153.2700	Sn16	−283.4193
Mg17	−38.9674	Mg17	−38.9147	Mg17	−38.8664
Al18	−43.6048	Al18	−43.5153	Al18	−43.4242

Table 2. (*Continued*).

Atom type	2-picoline → *Y-Si	Atom type	2-picoline → *Y-Ge	Atom type	2-picoline → *Y-Sn
Al8	−43.7532	Al8	−43.7111	Al8	−43.6978
Mg9	−38.7053	Mg9	−38.6701	Mg9	−38.6501
Si10	−48.2966	Ge10	−153.2712	Sn10	−283.4305
Mg11	−38.9638	Mg11	−38.9092	Mg11	−38.8567
Al12	−43.7545	Al12	−43.7164	Al12	−43.6948
Mg13	−38.7230	Mg13	−38.6731	Mg13	−38.6269
Al14	−43.3057	Al14	−43.2478	Al14	−43.1702
Si15	−48.0602	Ge15	−153.0194	Sn15	−283.1586
Al16	−43.6097	Al16	−43.5260	Al16	−43.4388
Si17	−48.3185	Ge17	−153.2727	Sn17	−283.4172
Mg18	−38.9481	Mg18	−38.8946	Mg18	−38.8520
Al19	−43.6090	Al19	−43.5166	Al19	−43.4294
Atom type	**3-picoline → *Y-Si**	**Atom type**	**3-picoline → *Y-Ge**	**Atom type**	**3-picoline → *Y-Sn**
Al8	−43.7246	Al8	−43.6836	Al8	−43.6548
Mg9	−38.7172	Mg9	−38.6724	Mg9	−38.6337
Si10	−48.3054	Ge10	−153.2696	Sn10	−283.4215
Mg11	−38.9386	Mg11	−38.8866	Mg11	−38.8567
Al12	−43.7254	Al12	−43.6885	Al12	−43.6676
Mg13	−38.7274	Mg13	−38.6861	Mg13	−38.6696
Al14	−43.3043	Al14	−43.2547	Al14	−43.1730
Si15	−48.0667	Ge15	−153.0218	Sn15	−283.1552
Al16	−43.5783	Al16	−43.4986	Al16	−43.4257
Si17	−48.3069	Ge17	−153.2718	Sn17	−283.433
Mg18	−38.9721	Mg18	−38.9132	Mg18	−38.8602
Al19	−43.6161	Al19	−43.5207	Al19	−43.4232
Atom type	**4-picoline → *Y-Si**	**Atom type**	**4-picoline → *Y-Ge**	**Atom type**	**4-picoline → *Y-Sn**
Al8	−43.7531	Al8	−43.72321	Al8	−43.6892
Mg9	−38.6963	Mg9	−38.6559	Mg9	−38.6105
Sn10	−48.3207	Ge10	−153.2842	Sn10	−283.4131
Mg11	−38.9586	Mg11	−38.9060	Mg11	−38.8429
Al12	−43.7227	Al12	−43.6807	Al12	−43.6533
Mg13	−38.7142	Mg13	−38.6753	Mg13	−38.6433
Al14	−43.3023	Al14	−43.2577	Al14	−43.1513
Sn15	−48.0718	Ge15	−153.0270	Sn15	−283.1463
Al16	−43.5906	Al16	−43.4921	Al16	−43.4153
Sn17	−48.3389	Ge17	−153.2830	Sn17	−283.4194
Mg18	−38.9153	Mg18	−38.8685	Mg18	−38.8356
Al19	−43.5522	Al19	−43.4668	Al19	−43.4193

Table 2. (*Continued*).

Atom type	2,4-lutidine → *Y-Si	Atom type	2,4-lutidine → *Y-Ge	Atom type	2,4-lutidine → *Y-Sn
Al9	−43.7221	Al9	−43.7298	Al9	−43.6618
Mg10	−38.7127	Mg10	−38.6854	Mg10	−38.6395
Si11	−48.3286	Ge11	−153.2770	Sn11	−283.4141
Mg12	−38.9369	Mg12	−38.8957	Mg12	−38.8555
Al13	−43.7453	Al13	−43.7243	Al13	−43.6687
Mg14	−38.7352	Mg14	−38.6900	Mg14	−38.6681
Al15	−43.2998	Al15	−43.3161	Al15	−43.1563
Si16	−48.0899	Ge16	−153.0344	Sn16	−283.1494
Al17	−43.5770	Al17	−43.5085	Al17	−43.4290
Si18	−48.3147	Ge18	−153.2780	Sn18	−283.4319
Mg19	−38.9704	Mg19	−38.9008	Mg19	−38.8602
Al20	−43.5921	Al20	−43.5114	Al20	−43.4272

In NQR, nuclei with spin ≥ 1, there is an electric quadrupole moment which is accompanied with non-spherical nuclear charge distributions. So, the nuclear charge distribution deviates from that of a sphere as the oblate or prolate form of the nucleus[105–108]. Moreover, the electric potential as the amount of work energy through transferring the electric charge from one site to another site in presence of electric field has been measured for pyridine, 2-picolone, 3-picoline, 4-picoline and 2,4-lutidine adsorbing onto Al-Mg-X (X = Si, Ge, Sn) nanoalloys surface using CAM-B3LYP/EPR-III, LANL2DZ, 6-31+G(d,p) level of theory. It is observed the effect of the substitution of aluminum atoms in Al-Mg nanoalloy surface with silicon, germanium and tin through resulted electric potential using NQR analysis (**Table 2**). It's obvious that the graph of Al-Mg is fluctuated by Si, Ge, Sn atoms in the related nanoalloys. In **Table 2**, it is remarked the regions of electric potential changes for all Al, Mg, Si, Ge, and Sn in Al-Mg-X (X = Mg, Ga, Si) versus atomic charge which are coated by pyridine and its family (**Table 2**).

The values of changes of charge density show a more important charge transfer from nitrogen heterocyclic inhibitors of pyridine, 2-picoline, 3-picoline, 4-picoline and 2,4-lutidine as the electron donor adsorbed onto Al-Mg-X (X = Si, Ge, Sn) nanoalloy surfaces which act as the electron acceptors (N → Al). In fact, Al sites in Al-Mg-X (X = Si, Ge, Sn) nanoalloy surfaces have higher interaction energy from Van der Waals' forces with pyridine and its nitrogen heterocyclic family that can make them highly stable toward coating information on the surface.

It is assumed that the priority for selecting the surface binding of N-atom in pyridine, 2-picoline, 3-picoline, 4-picoline and 2,4-lutidine in adsorption sites can be impacted by the existence of close atoms of magnesium, silicon, germanium and tin in the Al-Mg-X (X = Si, Ge, Sn) surfaces.

3.3. Infrared spectroscopy

The IR computations are done for three aluminum nanoalloys containing Al-Mg-Si, Al-Mg-Ge, Al-Mg-Sn, and the organic heterocyclic inhibitors including pyridine, 2-picoline, 3-picoline, 4-picoline and 2,4-lutidine adsorbed onto these nanoalloys surface. Therefore, it has been modeled the several complexes including pyridine → Al-Mg-Si, pyridine → Al-Mg-Ge, pyridine → Al-Mg-Sn; 2-picoline → Al-Mg-Si, 2-picoline → Al-Mg-Ge, 2-picoline → Al-Mg-Sn; 3-picoline → Al-Mg-Si, 3-picoline → Al-Mg-Ge, 3-picoline → Al-Mg-Sn; 4-picoline → Al-Mg-Si, 4-picoline → Al-Mg-Ge, 4-picoline → Al-Mg-Sn; and 2,4-lutidine → Al-Mg-Si, 2,4-lutidine → Al-Mg-Ge, 2,4-lutidine → Al-Mg-Sn. These structures are computed at CAM-B3LYP function accompanying LANL2DZ, 6-31+G (d,p), EPR-III basis sets (**Table 3**).

Table 3. The Physicochemical properties of adsorption for pyridine, 2-picoline, 3-picoline, 4-picoline and 2,4-lutidine as corrosion inhibitors on the aluminum nanoalloys surface including Al-Mg-Si, Al-Mg-Ge and Al-Mg-Sn at 300 K.

Compound	$\Delta E° \times 10^{-4}$ (kcal/mol)	$\Delta H° \times 10^{-4}$ (kcal/mol)	$\Delta G° \times 10^{-4}$ (kcal/mol)	S° (cal/K.mol)	Dipole moment (Debye)	$R_{N\text{-}Al}$ (Å)
Al-Mg-Si	−177.5928	−177.5928	−177.5950	75.321	1.7232	-
Al-Mg-Ge	−512.9296	−512.9295	−512.9319	79.090	1.5308	-
Al-Mg-Sn	−124.6274	−124.6274	−124.6276	79.866	2.2570	-
Pyridine	−15.3793	−15.3792	−15.3813	68.627	2.0338	-
Pyridine → Al-Mg-Si	−192.9530	−192.9530	−192.9557	91.157	2.4712	1.9295
Pyridine → Al-Mg-Ge	−525.5452	−525.5452	−525.5479	92.175	1.9259	1.9293
Pyridine → Al-Mg-Sn	−1261.6266	−1261.6266	−1261.6293	91.695	2.9003	1.9300
2-picoline	−17.8155	−17.8154	−17.8176	73.692	1.7413	-
2-picoline → Al-Mg-Si	−195.3850	−195.3857	−195.3876	88.761	2.0490	1.9298
2-picoline → Al-Mg-Ge	−527.9771	−527.9770	−527.9800	98.159	1.6681	1.9297
2-picoline → Al-Mg-Sn	−1264.0571	−1264.0570	−1264.0598	94.310	2.8543	1.9305
3-picoline	−17.8154	−17.8153	−17.8175	73.725	2.2156	-
3-picoline → Al-Mg-Si	−195.3898	−195.3898	−195.3924	88.868	2.7985	1.9298
3-picoline → Al-Mg-Ge	−527.9835	−527.9834	−527.9861	90.872	2.4932	1.9297
3-picoline → Al-Mg-Sn	−1264.0664	−1264.0663	−1264.0691	94.245	3.3364	1.9302
4-picoline	−17.8154	−17.8154	−17.8176	73.717	2.4672	-
4-picoline → Al-Mg-Si	−195.3848	−195.3847	−195.3873	88.658	3.9757	1.9298
4-picoline → Al-Mg-Ge	−527.9762	−527.9761	−527.9789	92.459	2.8767	1.9297
4-picoline → Al-Mg-Sn	−1264.0539	−1264.0539	−1264.0567	94.969	4.1486	1.9304
2,4-lutidine	−20.2516	−20.2515	−20.2539	78.728	2.1610	-
2,4-lutidine→ Al-Mg-Si	−197.8160	−197.8159	−197.8188	94.990	3.9424	1.9299
2,4-lutidine→ Al-Mg-Ge	−530.4323	−530.4322	−530.4351	97.365	2.0410	1.9296
2,4-lutidine→ Al-Mg-Sn	−1266.4886	−1266.4885	−1266.4913	94.545	4.2363	1.9302

Figure 2a–e results that this conservative surface contains an [inhibitor → Al-Mg-X (X = Si, Ge, Sn)] complexes. The maximum IR spectrum for each of these materials is observed in the frequency between 500 cm^{-1}–3500 cm^{-1} by the sharpest peaks about 3100 cm^{-1}, 3350 cm^{-1}, 1550 cm^{-1}, 1550 cm^{-1}, and 3075 cm^{-1}, for pyridine → Al-Mg-X, 2-picoline → Al-Mg-X, 3-picoline → Al-Mg-X, 4-picoline → Al-Mg-X and 2,4-lutidine → Al-Mg-X, respectively (**Figure 2a–e**).

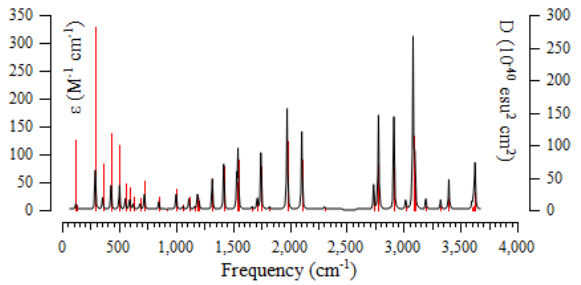

(a)

Figure 2. (*Continued*).

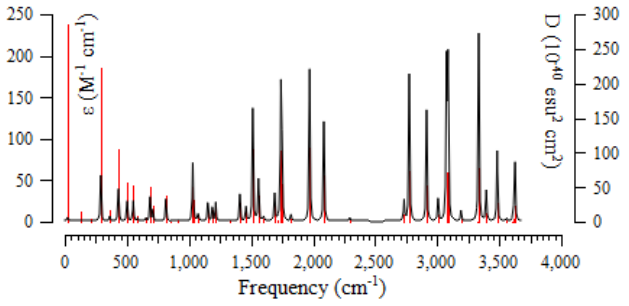

(b)

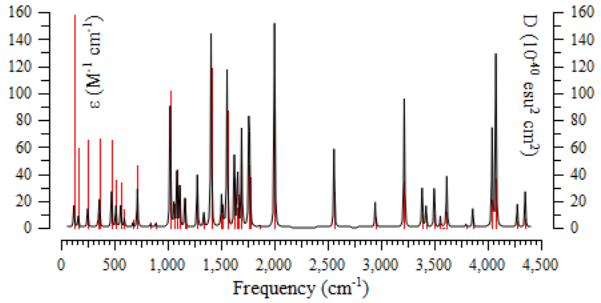

(c)

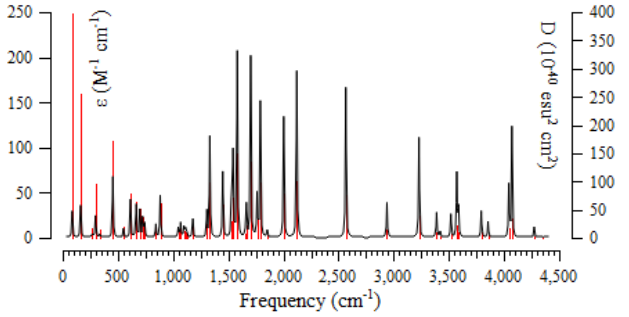

(d)

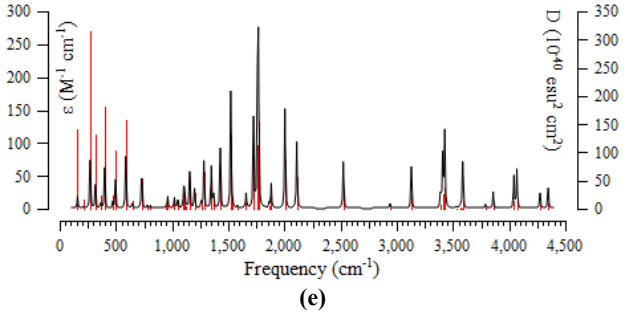

(e)

Figure 2. Diagram of IR spectra for **(a)** pyridine→ Al-Mg-X; **(b)** 2-picoline → Al-Mg-X; **(c)** 3-picoline → Al-Mg-X; **(d)** 4-picoline → Al-Mg-X and **(e)** 2,4-lutidine → Al-Mg-X adsorbed on the Al-Si surface using CAM-B3LYP/EPR-III, LANL2DZ,6-31+G(d,p) calculations. Note: (X = Si, Ge, Sn).

The correctness of the selected isotherm for the adsorption process of pyridine → Al-Mg-Si, pyridine → Al-Mg-Ge, pyridine → Al-Mg-Sn; 2-picoline → Al-Mg-Si, 2-picoline → Al-Mg-Ge, 2-picoline → Al-Mg-Sn; 3-picoline → Al-Mg-Si, 3-picoline → Al-Mg-Ge, 3-picoline → Al-Mg-Sn; 4-picoline → Al-Mg-Si, 4-picoline → Al-Mg-Ge, 4-picoline → Al-Mg-Sn; and 2,4-lutidine → Al-Mg-Si, 2,4-lutidine → Al-Mg-Ge, 2,4-lutidine → Al-Mg-Sn is reported in **Figure 3**.

The value of inhibitor adsorption on the Al-nanoalloys is measured by the ΔG^{o}_{ads} parameter.

$$\Delta G^{o}_{ads} = \Delta G^{o}_{inh\rightarrow \mathrm{Al-Mg-X}} - \left(\Delta G^{o}_{inh} + \Delta G^{o}_{\mathrm{Al-Mg-X}}\right);\ \mathrm{X = Si, Ge, Sn} \quad (8)$$

It is predicted that the adsorption of the inhibitor on the Al-Mg-X (X = Si, Ge, Sn) nanoalloys surface

might be physical and chemical nature (**Table 3**). As shown in **Table 3**, all the computed ΔG^{o}_{ads} amounts are very close, which exhibits the agreement of the evaluated data by all methods and the validity of the computations.

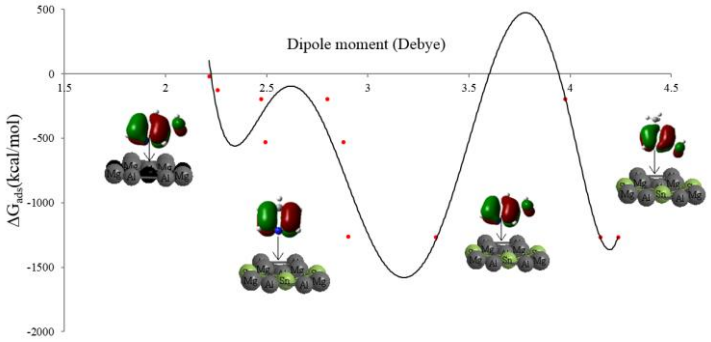

Figure 3. The Gibbs free energy for adsorption of pyridine and its derivatives as corrosion inhibitors on the aluminum nanoalloys consisting of Al-Mg-Si, Al-Mg-Ge and Al-Mg-Sn versus dipole moment (Debye).

3.4. Potential energy (PE) of interatomic interaction

The interatomic potential explains the interaction between a pair of atoms or the interaction of an atom with a group of atoms in a condensed phase. When binding happens, we can observe the potential having both an attractive and a repulsive component. Accompanying the Equation (9), it is investigated the Morse potential as follows[109]:

$$V_{\mathrm{M}}(r) = D_e(e^{-2\alpha(r-r_e)} - 2e^{-\alpha(r-r_e)}) \quad (9)$$

where D_e is the equilibrium bond energy and r_e the bond interval. So, the optimized PE of interatomic interaction for pyridine → Al-Mg-Si, pyridine → Al-Mg-Ge, pyridine → Al-Mg-Sn; 2-picoline → Al-Mg-Si, 2-picoline → Al-Mg-Ge, 2-picoline → Al-Mg-Sn; 3-picoline → Al-Mg-Si, 3-picoline → Al-Mg-Ge, 3-picoline → Al-Mg-Sn; 4-picoline → Al-Mg-Si, 4-picoline → Al-Mg-Ge, 4-picoline → Al-Mg-Sn; and 2,4-lutidine → Al-Mg-Si, 2,4-lutidine → Al-Mg-Ge, 2,4-lutidine → Al-Mg-Sn (**Table 3**).

Then, the interval between nitrogen atom in benzotriazole, oxygen atom in 8-hydroxyquinoline, and sulfur atom in in pyridine, 2-picoline, 3-picoline, 4-picoline and 2,4-lutidine, respectively, with aluminum in Al-Mg-X (X = Si, Ge, Sn) nanoalloys nanosurface is estimated (**Table 3** and **Figure 4**).

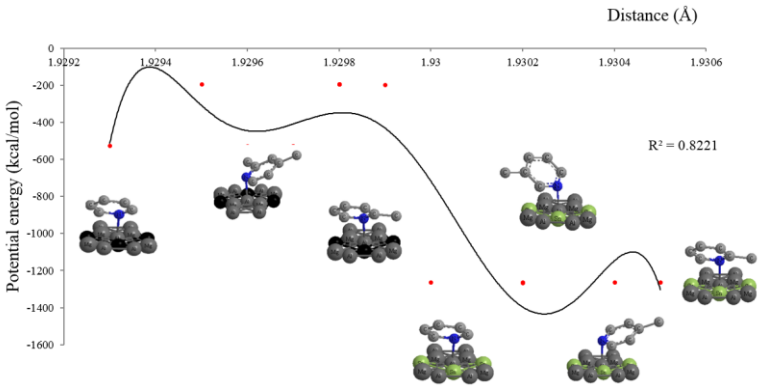

Figure 4. The graph of PE (kcal/mol) of interatomic interaction versus interval (Å) of N atom in pyridine and its family with aluminum in Al-Mg-X (X = Si, Ge, Sn) nanoalloys surface.

Based on **Figure 4**, it can be assumed that for the [heterocyclic inhibitors → (Al-Mg-X)] nanoalloys nanosurface, Lennar Jones potential as an intermolecular pair potential can be described[110]:

$$V_{LJ}(r) = 4\varepsilon\left[\left(\frac{\sigma}{r}\right)^{12} - \left(\frac{\sigma}{r}\right)^{6}\right] \quad (10)$$

where ε is the profundity of the potential well and σ is the interval at which the potential = 0. The attractive term proportional to $\frac{1}{r^6}$ in the potential comes from the balancing the van der vdW forces, while the $\frac{1}{r^{12}}$ repulsive term is much more approximate[111].

Regarding the enhanced molecule-sensing property of non-metal/metalloid/metal-doped Al–Mg surface, the effective sensitized region can be accumulated of the dopant, which contributed to the exigence to preserve a defined quantity of the doped Si, Ge and Sn.

4. Conclusion

In this research, the competence of the organic heterocyclic inhibitors as the aluminum nanoalloy coating is investigated through the thermoelectric traits and specifications of the environmental condition extracted from NMR, NQR, IR spectra, electric potential, charge distribution and other quantum data analysis which have been accomplished on pyridine → Al-Mg-Si, pyridine → Al-Mg-Ge, pyridine → Al-Mg-Sn; 2-picoline → Al-Mg-Si, 2-picoline → Al-Mg-Ge, 2-picoline → Al-Mg-Sn; 3-picoline → Al-Mg-Si, 3-picoline → Al-Mg-Ge, 3-picoline → Al-Mg-Sn; 4-picoline → Al-Mg-Si, 4-picoline → Al-Mg-Ge, 4-picoline → Al-Mg-Sn; and 2,4-lutidine → Al-Mg-Si, 2,4-lutidine → Al-Mg-Ge, 2,4-lutidine → Al-Mg-Sn.

Regarding NMR results, the sharpest peaks for inhibitors → Al-Mg-X are approximately between 10 ppm–100 ppm. Moreover, NQR approach has indicated that the regions of electric potential changes for all Al, Mg, Si, Ge, and Sn in Al-Mg-X (X = Mg, Ga, Si) versus atomic charge which are coated by pyridine and its family. In addition, the maximum IR spectrum for each of these materials is observed in the frequency between 500 cm^{-1}–3500 cm^{-1} by the sharpest peaks about 3100 cm^{-1}, 3350 cm^{-1}, 1550 cm^{-1}, 1550 cm^{-1}, and 3075 cm^{-1}, for pyridine → Al-Mg-X, 2-picoline → Al-Mg-X, 3-picoline → Al-Mg-X, 4-picoline → Al-Mg-X and 2,4-lutidine → Al-Mg-X, respectively.

An elaborate investigation for the mechanism of local minima in the adsorption potential energy landscape represents that the intact pyridine, 2-picoline, 3-picoline, 4-picoline and 2,4-lutidine adsorb with the aromatic ring parallel to the Al-Mg-X (X = Si, Ge, Sn) nanoalloys surface. In the preferred path, these organic inhibitors remain parallel to the surface while performing small single rotational steps with a carbon-carbon double bond hinged above a single aluminum atom in Al-Mg-Si, Al-Mg-Ge, and Al-Mg-Sn. The most eventual adsorption state of the inhibitors is one in which the nitrogen of the pyridine ring is near the Al atom in Al-Mg-Si, Al-Mg-Ge, and Al-Mg-Sn in an inclined state. The excellent molecule sensing performance is attributed to increased atom vacancies after doping and the increased adsorption of the molecules. This work presents an approach to synthesize other uniform metal-doped Al–Mg nanosurface and is also believed to be further extended to prepare other doped metal surface semiconductor nanostructures.

Author contributions

Conceptualization and idea, FM; methodology, FM and MM; software, FM and MM; validation, FM; formal analysis, FM and MM; resources, MM; investigation, FM and MM; data curation, FM and MM; writing—original draft preparation, FM; writing—review and editing, MM; visualization, FM and MM; supervision FM; project administration, FM. All authors have read and agreed to the published version of the manuscript.

Acknowledgments

In successfully completing this paper and its research, the authors are grateful to Kastamonu University.

Conflict of interest

The authors declare no conflict of interest.

References

1. He H, Yang T, Ren Y, et al. Experimental investigation on the formability of Al-Mg alloy 5052 sheet by tensile and cupping test. *Materials* 2022; 15(24): 8949. doi: 10.3390/ma15248949
2. Chen Y, Yang Y, Wang H, et al. Finite element analysis of fluid–structure interaction in a model of an L-type Mg alloy stent-stenosed coronary artery system. *Metals* 2022; 12(7): 1176. doi: 10.3390/met12071176
3. Bao G, Fan Q, Ge D, et al. In vitro and in vivo studies on magnesium alloys to evaluate the feasibility of their use in obstetrics and gynecology. *Acta Biomaterialia* 2019; 97: 623–636. doi: 10.1016/j.actbio.2019.08.001
4. Alaneme KK, Kareem SA, Olajide JL, et al. Computational biomechanical and biodegradation integrity assessment of Mg-based biomedical devices for cardiovascular and orthopedic applications: A review. *International Journal of Lightweight Materials and Manufacture* 2022; 5(2): 251–266. doi: 10.1016/j.ijlmm.2022.02.003
5. Mollaamin F, Monajjemi M, Sakhaeinia H. Nano-metallic semiconductor towards the vibrational analysis and harmonic linear combination. *Russian Journal of Physical Chemistry A* 2022; 96(5): 1051–1061. doi: 10.1134/s0036024422050090
6. Hong Hue DT, Tran VK, Nguyen VL, et al. High strain-rate effect on microstructure evolution and plasticity of Aluminum 5052 alloy nano-multilayer: A molecular dynamics study. *Vacuum* 2022; 201: 111104. doi: 10.1016/j.vacuum.2022.111104
7. Liu Y, Liu Z, Zhou G, et al. Microstructures and properties of Al-Mg alloys manufactured by WAAM-CMT. *Materials* 2022; 15(15): 5460. doi: 10.3390/ma15155460
8. Ren Z, Zhao Y, Han G, et al. Laser-Arc hybrid cladding of Al-Mg alloy coating on AZ80 Mg alloy: Effect of laser beam oscillations amplitude. *Materials* 2022; 15(20): 7272. doi: 10.3390/ma15207272
9. Monajjemi M, Khaleghian M, Tadayonpour N, et al. The effect of different solvents and temperatures on stability of single-walled carbon nanotube: A QM/MD study. *Int. J. Nanosci.* 2010; 9(5): 517–529. doi: 10.1142/S0219581X10007071
10. Tan J, Ramakrishna S. Applications of magnesium and its alloys: A review. *Applied Sciences* 2021; 11(15): 6861. doi: 10.3390/app11156861
11. Yang W, Jung YG, Kwak T, et al. Microstructure and mechanical properties of an Al-Mg-Si-Zr alloy processed by L-PBF and subsequent heat treatments. *Materials* 2022; 15(15): 5089. doi: 10.3390/ma15155089
12. Ali SA, Mazumder MAJ, Nazal MK, Al-Muallem HA. Assembly of succinic acid and isoxazolidine motifs in a single entity to mitigate CO_2 corrosion of mild steel in saline media. *Arabian Journal of Chemistry* 2020; 13(1): 242–257. doi: 10.1016/j.arabjc.2017.04.005
13. Rometsch PA, Zhu Y, Wu X, Huang A. Review of high-strength Aluminium alloys for additive manufacturing by laser powder bed fusion. *Materials & Design* 2022; 219: 110779. doi: 10.1016/j.matdes.2022.110779
14. Dong Z, Xu M, Guo H, et al. Microstructural evolution and characterization of AlSi10Mg alloy manufactured by selective laser melting. *Journal of Materials Research and Technology* 2022; 17: 2343–2354. doi: 10.1016/j.jmrt.2022.01.129
15. Otani Y, Sasaki S. Effects of the addition of silicon to 7075 Aluminum alloy on microstructure, mechanical properties, and selective laser melting processability. *Materials Science and Engineering: A* 2020; 777: 139079. doi: 10.1016/j.msea.2020.139079
16. Pan W, Zhai Z, Liu Y, et al. Research on microstructure and cracking behavior of Al-6.2Zn-2Mg-xSc-xZr alloy fabricated by selective laser melting. *Crystals* 2022; 12(10): 1500. doi: 10.3390/cryst12101500
17. Dieringa H, StJohn D, Pérez Prado MT, Kainer KU. Latest developments in the field of Magnesium alloys and their applications. *Frontiers in Materials* 2021; 8. doi: 10.3389/fmats.2021.726297
18. Mollaamin F, Monajjemi M. Tailoring and functionalizing the graphitic-like GaN and GaP nanostructures as selective sensors for NO, NO_2, and NH_3 adsorbing: A DFT study. *Journal of Molecular Modeling* 2023; 29(6): 170. doi: 10.1007/s00894-023-05567-8
19. Mollaamin F, Ilkhani A, Sakhaei N, et al. Thermodynamic and solvent effect on dynamic structures of nano bilayer-cell membrane: Hydrogen bonding study. *J. Comput. Theor. Nanosci.* 2015; 12(10): 3148–3154. doi: 10.1166/jctn.2015.4092
20. Das AK. Recent trends in laser cladding and alloying on magnesium alloys: A review. *Materials Today: Proceedings* 2022; 51: 723–727. doi: 10.1016/j.matpr.2021.06.217
21. Yao XY, Tang JC, Zhou YH, et al. Selective laser melting of an Mg/Metallic Glass hybrid for significantly improving chemical and mechanical performances. *Applied Surface Science* 2022; 580: 152229. doi: 10.1016/j.apsusc.2021.152229
22. Vončina M, Nagode A, Medved J, et al. Homogenisation efficiency assessed with microstructure analysis and hardness measurements in the EN AW 2011 Aluminium alloy. *Metals* 2021; 11(8): 1211. doi:

10.3390/met11081211
23. Kumar A, Pandey C. Autogenous laser-welded dissimilar joint of ferritic/martensitic P92 steel and inconel 617 alloy: Mechanism, microstructure, and mechanical properties. *Archives of Civil and Mechanical Engineering* 2022; 22(1): 39. doi: 10.1007/s43452-021-00365-6
24. Xu Y, Zhang Z, Zhao P, et al. Effects of ESMT on microstructure and mechanical properties of Al-8Zn-2Mg-1.5Cu-0.15Sc-0.15Zr cast alloy in squeeze casting process. *Crystals* 2022; 12(7): 996. doi: 10.3390/cryst12070996
25. Jiang L, Zhang Z, Wang Y, et al. Effects of Sc microalloying on microstructure and properties of As-Extruded Al-5Mg alloy. *Crystals* 2022; 12(7): 939. doi: 10.3390/cryst12070939
26. Li S, Bai Y, Zhang Z, Jiang L. Effects of vacuum-stirring purification process on Al-6Mg alloy melt. *Crystals* 2022; 12(5): 675. doi: 10.3390/cryst12050675
27. Jiang L, Zhang Z, Bai Y, et al. Study on Sc microalloying and strengthening mechanism of Al-Mg alloy. *Crystals* 2022; 12(5): 673. doi: 10.3390/cryst12050673
28. Zhai Z, Pan W, Liang B, et al. Cracking behavior, microstructure and properties of selective laser melted Al-Mn-Mg-Sc-Zr alloy. *Crystals* 2022; 12(4): 565. doi: 10.3390/cryst12040565
29. Chen M, Bai Y, Zhang Z, Zhao H. The preparation of high-volume fraction SiC/Al composites with high thermal conductivity by vacuum pressure infiltration. *Crystals* 2021; 11(5): 515. doi: 10.3390/cryst11050515
30. Zhang F, Zhang J, Ni H, et al. Optimization of AlSi10MgMn alloy heat treatment process based on orthogonal test and grey relational analysis. *Crystals* 2021; 11(4): 385. doi: 10.3390/cryst11040385
31. Khaleghian M, Zahmatkesh M, Mollaamin F, et al. Investigation of Solvent Effects on Armchair Single-Walled Carbon Nanotubes: A QM/MD Study. *Fuller. Nanotub. Carbon Nanostructures* 2011; 19(4): 251–261. doi: 10.1080/15363831003721757
32. Galyshev S. On the strength of the CF/Al-wire depending on the fabrication process parameters: Melt temperature, time, ultrasonic power, and thickness of carbon fiber coating. *Metals* 2021; 11(7): 1006. doi: 10.3390/met11071006
33. Mollaamin F. Features of parametric point nuclear magnetic resonance of metals implantation on boron nitride nanotube by density functional theory/electron paramagnetic resonance. *Journal of Computational and Theoretical Nanoscience* 2014; 11(11): 2393–2398. doi: 10.1166/jctn.2014.3653
34. Wang X, Chen Z, Ma T, et al. Evolution of primary and eutectic Si phase and mechanical properties of Al_2O_3/Al-20Si composites under high pressure. *Crystals* 2021; 11(4): 364. doi: 10.3390/cryst11040364
35. Zadeh MAA, Lari H, Kharghanian L, et al. Density functional theory study and anti-cancer properties of shyshaq plant: In view point of nano biotechnology. *Journal of Computational and Theoretical Nanoscience* 2015; 12(11): 4358–4367. doi: 10.1166/jctn.2015.4366
36. Zhao K, Gao T, Yang H, et al. Enhanced grain refinement and mechanical properties of a high–strength Al–Zn–Mg–Cu–Zr alloy induced by TiC nano–particles. *Materials Science and Engineering: A* 2021; 806: 140852. doi: 10.1016/j.msea.2021.140852
37. Tahan A, Mollaamin F, Monajjemi M. Thermochemistry and NBO analysis of peptide bond: Investigation of basis sets and binding energy. *Russian Journal of Physical Chemistry A* 2009; 83(4): 587–597. doi: 10.1134/s003602440904013x
38. Xiao H, Li Y, Geng J, et al. Effects of nano-sized TiB_2 particles and Al_3Zr dispersoids on microstructure and mechanical properties of Al-Zn-Mg-Cu based materials. *Transactions of Nonferrous Metals Society of China* 2021; 31(8): 2189–2207. doi: 10.1016/S1003-6326(21)65648-0
39. Khalili Hadad B, Mollaamin F, Monajjemi M, Biophysical chemistry of macrocycles for drug delivery: A theoretical study. *Russ. Chem. Bulletin.* 2011; 60: 238–241. doi: 10.1007/s11172-011-0039-5
40. Monajjemi M, Mollaamin F, Shojaei S, An overview on Coronaviruses family from past to Covid-19: Introduce some inhibitors as antiviruses from Gillan's plants Biointerface. *Res. Appl. Chem.* 2020; 10(3): 5575–5585. doi: 10.33263/BRIAC103.575585
41. Louis H, Chukwuemeka K, Agwamba EC, et al. Molecular simulation of Cu, Ag, and Au-decorated Si-doped graphene quantum dots (Si@QD) nanostructured as sensors for SO_2 trapping. *Journal of Molecular Graphics and Modelling* 2023; 124: 108551. doi: 10.1016/j.jmgm.2023.108551
42. Melamed Y, Maity N, Meshi L, Eliaz N. Electroplating of pure Aluminum from [HMIm][TFSI]–$AlCl_3$ room-temperature ionic liquid. *Coatings* 2021; 11(11): 1414. doi: 10.3390/coatings11111414
43. Siddesh Kumar NM, Dhruthi, Pramod GK, et al. A critical review on heat treatment of Aluminium alloys. *Materials Today: Proceedings* 2022; 58: 71–79. doi: 10.1016/j.matpr.2021.12.586
44. Fang X, Li Y, Zheng Q, et al. Theoretical prediction of structural, mechanical, and thermophysical properties of the precipitates in 2xxx series Aluminum alloy. *Metals* 2022; 12(12): 2178. doi: 10.3390/met12122178
45. Mollaamin F, Monajjemi M, Salemi S, et al. A dielectric effect on normal mode analysis and symmetry of BNNT Nanotube. *Fuller. Nanotub. Carbon Nanostructures* 2011; 19(3): 182–196. doi: 10.1080/15363831003782932
46. Würger T, Feiler C, Vonbun-Feldbauer GB, et al. A first-principles analysis of the charge transfer in magnesium corrosion. *Scientific Reports* 2020; 10(1): 15006. doi: 10.1038/s41598-020-71694-4
47. Ma H, Chen LJ, Guo LQ, et al. First-principles calculation of Al-Cu-Mg alloy strengthening phase. *Advanced Materials Research* 2015; 1096: 109–113. doi: 10.4028/www.scientific.net/amr.1096.109

48. Zhou L, Su K, Wang Y, et al. First-principles study of the properties of Li, Al and Cd doped Mg alloys. *Journal of Alloys and Compounds* 2014; 596: 63–68. doi: 10.1016/j.jallcom.2014.01.199
49. Carrasco J, Hodgson A, Michaelides A. A molecular perspective of water at metal interfaces. *Nature Mater* 2012; 11(8): 667–674. doi: 10.1038/nmat3354
50. Chen J, Schusteritsch G, Pickard CJ, et al. Two dimensional ice from first principles: Structures and phase transitions. *Physical Review Letters* 2016; 116(2): 025501. doi: 10.1103/physrevlett.116.025501
51. Louis H, Benjamin I, Iloanya AC, et al. Functionalized (–HCO, –OH, –NH_2) Iridium-doped graphene (Ir@Gp) nanomaterials for enhanced delivery of Piroxicam: Insights from quantum chemical calculations. *Journal of Molecular Liquids* 2023; 383: 122068. doi: 10.1016/j.molliq.2023.122068
52. Oyo-Ita I, Louis H, Nsofor VC, et al. Studies on transition metals (Rh, Ir, Co) doped silicon carbide nanotubes (SiCNT) for the detection and adsorption of acrolein: Insight from DFT approach. *Materials Science and Engineering: B* 2023; 296: 116668. doi: 10.1016/j.mseb.2023.116668
53. Calle-Vallejo F, Martínez JI, García-Lastra JM, et al. Fast prediction of adsorption properties for platinum nanocatalysts with generalized coordination numbers. *Angewandte Chemie International Edition* 2014; 53(32): 8316–8319. doi: 10.1002/anie.201402958
54. Akpe MA, Louis H, Gber TE, et al. Modeling of Cu, Ag, and Au-decorated $Al_{12}Se_{12}$ nanostructured as sensor materials for trapping of chlorpyrifos insecticide. *Computational and Theoretical Chemistry* 2023; 1226: 114218. doi: 10.1016/j.comptc.2023.114218
55. Greeley J, Nørskov JK. Electrochemical dissolution of surface alloys in acids: Thermodynamic trends from first-principles calculations. *Electrochimica Acta* 2007; 52(19): 5829–5836. doi: 10.1016/j.electacta.2007.02.082
56. Okon GA, Ogungbemiro FO, Louis H, et al. Single-atom transition metals (Rh, Ir, Co) doped silicon carbide nanotubes (SiCNT) as nonenzymatic nitrotyrosine (NTS) sensor: Insight from theoretical calculations. *Computational and Theoretical Chemistry* 2023; 1227: 114250. doi: 10.1016/j.comptc.2023.114250
57. Zhu X, Dong X, Blake P, Ji S. Improvement in as-cast strength of high pressure die-cast Al–Si–Cu–Mg alloys by synergistic effect of Q-$Al_5Cu_2Mg_8Si_6$ and θ-Al_2Cu phases. *Materials Science and Engineering: A* 2021; 802: 140612. doi: 10.1016/j.msea.2020.140612
58. Liu Y, Wen JC, Zhang XY, Huang YC. A comparative study on heterogeneous nucleation and mechanical properties of the fcc-Al/$L1_2$-Al_3M (M = Sc, Ti, V, Y, Zr, Nb) interface from first-principles calculations. *Physical Chemistry Chemical Physics* 2021; 23(8): 4718–4727. doi: 10.1039/d0cp05832g
59. Sun F, Zhang G, Liu H, et al. Effect of transition-elements substitution on mechanical properties and electronic structures of B2-AlCu compounds. *Results in Physics* 2021; 21: 103765. doi: 10.1016/j.rinp.2020.103765
60. Zhang S, Yi W, Zhong J, et al. Computer alloy design of Ti modified Al-Si-Mg-Sr casting alloys for achieving simultaneous enhancement in strength and ductility. *Materials* 2022; 16(1): 306. doi: 10.3390/ma16010306
61. Yi W, Liu G, Gao J, Zhang L. Boosting for concept design of casting aluminum alloys driven by combining computational thermodynamics and machine learning techniques. *Journal of Materials Informatics* 2021; 1(2). doi: 10.20517/jmi.2021.10
62. Yi W, Liu G, Lu Z, et al. Efficient alloy design of Sr-modified A356 alloys driven by computational thermodynamics and machine learning. *Journal of Materials Science & Technology* 2022; 112: 277–290. doi: 10.1016/j.jmst.2021.09.061
63. Chrominski W, Lewandowska M. Precipitation strengthening of Al-Mg-Si alloy subjected to multiple accumulative roll bonding combined with a heat treatment. *Materials & Design* 2022; 219: 110813. doi: 10.1016/j.matdes.2022.110813
64. Ji X, Zhang H, Luo S, et al. Microstructures and properties of Al–Mg–SI alloy overhead conductor by horizontal continuous casting and continuous extrusion forming process. *Materials Science and Engineering: A* 2016; 649: 128–134. doi: 10.1016/j.msea.2015.09.114
65. Sauvage X, Bobruk EV, Murashkin MY, et al. Optimization of electrical conductivity and strength combination by structure design at the nanoscale in Al–Mg–Si alloys. *Acta Materialia* 2015; 98: 355–366. doi: 10.1016/j.actamat.2015.07.039
66. Mei L, Chen XP, Huang GJ, Liu Q. Improvement of mechanical properties of a cryorolled Al-Mg-Si alloy through warm rolling and aging. *Journal of Alloys and Compounds* 2019; 777: 259–263. doi: 10.1016/j.jallcom.2018.11.012
67. Mollaamin F, Monajjemi M. Tribocorrosion framework of (Iron, Nickel, Zinc)-doped graphene nanosheet: New sights into sulfur dioxide and hydrogen sulfide removal using DFT/TD-DFT methods. *Journal of Bio- and Tribo-Corrosion* 2023; 9(3): 47. doi: 10.1007/s40735-023-00768-3
68. Murakami T, Matsuda K, Nagai T, et al. Aging behavior of Al-Mg-Ge alloys with different Mg_2Ge contents. *Advanced Materials Research* 2011; 409: 63–66. doi: 10.4028/www.scientific.net/amr.409.63
69. Bjørge R, Nakashima PNH, Marioara CD, et al. Precipitates in an Al–Mg–Ge alloy studied by aberration-corrected scanning transmission electron microscopy. *Acta Materialia* 2011; 59(15): 6103–6109. doi: 10.1016/j.actamat.2011.06.021
70. Kurihara K, Lobzenko I, Tsuru T, Serizawa A. Interaction between solute atoms and vacancies in Al-Mg-X (X = Si, Ge) alloys. *Journal of Japan Institute of Light Metals* 2022; 72(7): 427–429. doi: 10.2464/jilm.72.427

71. Galyshev S, Orlov V, Atanov B, et al. The effect of Tin content on the strength of a carbon Fiber/Al-Sn-matrix composite wire. *Metals* 2021; 11(12): 2057. doi: 10.3390/met11122057
72. Raghavan V. Al-Mg-Sn (Aluminum-Magnesium-Tin). *Journal of Phase Equilibria and Diffusion* 2010; 32(1): 57–60. doi: 10.1007/s11669-010-9798-1
73. Mollaamin F, Monajjemi M. Doping of graphene nanostructure with Iron, Nickel and Zinc as selective detector for the toxic gas removal: A density functional theory study. *C—Journal of Carbon Research* 2023; 9(1): 20. doi: 10.3390/c9010020
74. Abdel Rehim SS, Hassan HH, Amin MA. Chronoamperometric studies of pitting corrosion of Al and (Al–Si) alloys by halide ions in neutral sulphate solutions. *Corrosion Science* 2004; 46(8): 1921–1938. doi: 10.1016/j.corsci.2003.10.016
75. Davis JR. *Corrosion: Understanding the Basics*. ASM International; 2000. doi: 10.31399/asm.tb.cub.9781627082501
76. Mollaamin F, Monajjemi M. Corrosion inhibiting by some organic heterocyclic inhibitors through langmuir adsorption mechanism on the Al-X (X = Mg/Ga/Si) alloy surface: A study of quantum three-layer method of CAM-DFT/ONIOM. *Journal of Bio- and Tribo-Corrosion* 2023; 9(2): 33. doi: 10.1007/s40735-023-00751-y
77. Karplus M. Development of multiscale models for complex chemical systems: From $H+H_2$ to biomolecules (nobel lecture). *Angewandte Chemie International Edition* 2014; 53(38): 9992–10005. doi: 10.1002/anie.201403924
78. Levitt M. Birth and future of multiscale modeling for macromolecular systems (nobel lecture). *Angewandte Chemie International Edition* 2014; 53(38): 10006–10018. doi: 10.1002/anie.201403691
79. Warshel A. Multiscale modeling of biological functions: from enzymes to molecular machines (nobel lecture). *Angewandte Chemie International Edition* 2014; 53(38): 10020–10031. doi: 10.1002/anie.201403689
80. Senn HM, Thiel W. QM/MM methods for biomolecular systems. *Angewandte Chemie International Edition* 2009; 48(7): 1198–1229. doi: 10.1002/anie.200802019
81. Senn HM, Thiel W. QM/MM methods for biological systems In: Reiher M (editor). *Atomistic Approaches in Modern Biology: From Quantum Chemistry to Molecular Simulations*. Springer; 2007. Volume 268.
82. Shen AY, Wu SN, Chiu CT. Synthesis and cytotoxicity evaluation of some 8-hydroxyquinoline derivatives. *Journal of Pharmacy and Pharmacology* 1999; 51(5): 543–548. doi: 10.1211/0022357991772826
83. Luo M, Yao L, Wu Q, et al. A study on correlation between electronic structure and inhibition properties of five-membered dinitrogen heterocyclic compounds (Chinese). *Journal of Chinese Society for Corrosion and protection* 1996; 16(3): 195–200.
84. Mollaamin F, Shahriari S, Monajjemi M, Khalaj Z. Nanocluster of Aluminum lattice via organic inhibitors coating: A study of freundlich adsorption. *Journal of Cluster Science* 2022; 34(3): 1547–1562. doi: 10.1007/s10876-022-02335-1
85. Brandt F, Jacob CR. Systematic QM region construction in QM/MM calculations based on uncertainty quantification. *Journal of Chemical Theory and Computation* 2022; 18(4): 2584–2596. doi: 10.1021/acs.jctc.1c01093
86. Mashuga ME, Olasunkanmi LO, Ebenso EE. Experimental and theoretical investigation of the inhibitory effect of new pyridazine derivatives for the corrosion of mild steel in 1 M HCl. *Journal of Molecular Structure* 2017; 1136: 127–139. doi: 10.1016/j.molstruc.2017.02.002
87. Guimarães TAS, da Cunha JN, de Oliveira GA, et al. Nitrogenated derivatives of furfural as green corrosion inhibitors for mild steel in HCl solution. *Journal of Materials Research and Technology* 2020; 9(4): 7104–7122. doi: 10.1016/j.jmrt.2020.05.019
88. Mollaamin F, Monajjemi M. Application of DFT and TD-DFT on langmuir adsorption of nitrogen and sulfur heterocycle dopants on an Aluminum surface decorated with Magnesium and Silicon. *Computation* 2023; 11(6): 108. doi: 10.3390/computation11060108
89. Bakhshi K, Mollaamin F, Monajjemi M. Exchange and correlation effect of hydrogen chemisorption on nano V(100) surface: A DFT study by generalized gradient approximation (GGA). *Journal of Computational and Theoretical Nanoscience* 2011; 8(4): 763–768. doi: 10.1166/jctn.2011.1750
90. Mollaamin F, Monajjemi M. Molecular modelling framework of metal-organic clusters for conserving surfaces: Langmuir sorption through the TD-DFT/ONIOM approach. *Molecular Simulation* 2022; 49(4): 365–376. doi: 10.1080/08927022.2022.2159996
91. Kohn W, Becke AD, Parr RG. Density functional theory of electronic structure. *The Journal of Physical Chemistry* 1996; 100(31): 12974–12980. doi: 10.1021/jp960669l
92. Ladeira ACQ, Ciminelli VST, Duarte HA, et al. Mechanism of anion retention from EXAFS and density functional calculations: arsenic (V) adsorbed on gibbsite. *Geochimica et Cosmochimica Acta* 2001; 65(8): 1211–1217. doi: 10.1016/S0016-7037(00)00581-0
93. Mollaamin F, Monajjemi M. Transition metal (X = Mn, Fe, Co, Ni, Cu, Zn)-doped graphene as gas sensor for CO_2 and NO_2 detection: A molecular modeling framework by DFT perspective. *Journal of Molecular Modeling* 2023; 29(4): 119. doi: 10.1007/s00894-023-05526-3
94. Koch W, Holthausen MC. *A Chemist's Guide to Density Functional Theory*. Wiley-VCH; 2001. doi: 10.1002/3527600043

95. Hohenberg P, Kohn W. Inhomogeneous electron gas. *Physical Review* 1964; 136: B864–B871. doi: 10.1103/physrev.136.b864
96. Kohn W, Sham LJ. Self-consistent equations including exchange and correlation effects. *Physical Review* 1965; 140: A1133–A1138. doi: 10.1103/physrev.140.a1133
97. Becke AD. Density-functional thermochemistry. III. The role of exact exchange. *The Journal of Chemical Physics* 1993; 98(7): 5648–5652. doi: 10.1063/1.464913
98. Lee C, Yang W, Parr RG. Development of the Colle-Salvetti correlation-energy formula into a functional of the electron density. *Physical Review B* 1988; 37(2): 785–789. doi: 10.1103/physrevb.37.785
99. Mollaamin F, Monajjemi M. Electric and magnetic evaluation of Aluminum-Magnesium nanoalloy decorated with Germanium through heterocyclic carbenes adsorption: A density functional theory study. *Russian Journal of Physical Chemistry B* 2023; 17(3): 658–672. doi: 10.1134/s1990793123030223
100. Monajjemi M, Baie MT, Mollaamin F. Interaction between threonine and cadmium cation in $[Cd(Thr)_n]^{2+}$ (n = 1–3) complexes: Density functional calculations. *Russian Chemical Bulletin* 2010; 59(5): 886–889. doi: 10.1007/s11172-010-0181-5
101. Cramer CJ. *Essentials of Computational Chemistry: Theories and Models*, 2nd ed. Wiley; 2004.
102. Vosko SH, Wilk L, Nusair M. Accurate spin-dependent electron liquid correlation energies for local spin density calculations: A critical analysis. *Canadian Journal of Physics* 1980; 58(8): 1200–1211. doi: 10.1139/p80-159
103. Frisch MJ, Trucks GW, Schlegel HB, et al. *Gaussian 16, Revision C.01*. Gaussian, Inc.; 2016.
104. Dennington R, Keith TA, Millam JM. *GaussView, Version 6.06.16*. Semichem Inc.; 2016.
105. Smith JAS. Nuclear quadrupole resonance spectroscopy. General principles. *Journal of Chemical Education* 1971; 48(1): 39. doi: 10.1021/ed048p39
106. Allen N. Appendix K: Nuclear quadrupole resonance. In: Jacqueline MG, Lockwood JR (editors). *Alternatives for Landmine Detection*. Rand Corporation; 2003.
107. Mollaamin F, Monajjemi M. Graphene-based resistant sensor decorated with Mn, Co, Cu for nitric oxide detection: Langmuir adsorption & DFT method. *Sensor Review* 2023; 43(4): 266–279. doi: 10.1108/sr-03-2023-0040
108. Young HA, Freedman RD. *Sears and Zemansky's University Physics with Modern Physics*, 13th ed. Addison-Wesley; 2011. p. 754.
109. Monajjemi M, Mollaamin F, Gholami MR, et al. Quantum chemical parameters of some organic corrosion inhibitors, pyridine, 2-Picoline 4-Picoline and 2,4-Lutidine, adsorption at Aluminum surface in hydrocholoric and nitric acids and comparison between two acidic media. *Main Group Metal Chemistry* 2003; 26(6): 349–361. doi: 10.1515/mgmc.2003.26.6.349
110. Heinz H, Vaia RA, Farmer BL, Naik RR. Accurate simulation of surfaces and interfaces of face-centered cubic metals using 12−6 and 9−6 Lennard-Jones potentials. *The Journal of Physical Chemistry C* 2008; 112(44): 17281–17290. doi: 10.1021/jp801931d
111. Mollaamin F, Monajjemi M. In Silico-DFT investigation of nanocluster alloys of Al-(Mg, Ge, Sn) coated by nitrogen heterocyclic carbenes as corrosion inhibitors. *Journal of Cluster Science* 2023; 34(6): 2901–2918. doi: 10.1007/s10876-023-02436-5